A Silicon Nanowire as a Spectrally Tunable Light-Driven Nanomotor

Jizhuang Wang, Ze Xiong, Xiaojun Zhan, Baohu Dai, Jing Zheng, Jun Liu, and Jinyao Tang*

Over the last decades, scientists have endeavored to develop nanoscopic machines and envisioned that these tiny machines could be exploited in biomedical applications and novel material fabrication. Here, a visible-/near-infrared light-driven nanomotor based on a single silicon nanowire is reported. The silicon nanomotor harvests energy from light and propels itself by the self-electrophoresis mechanism. Due to the high efficiency, the silicon nanowire can be readily driven by visible and near-infrared illumination at ultralow light intensity ($\approx$3 mW cm^{-2}). The experimental study and numerical simulation also show that the detailed structure around the concentrated reaction center determines the migration behavior of the nanomotor. Importantly, due to the optical resonance inside the silicon nanowire, the spectral response of the nanowire-based nanomotor can be readily modulated by the nanowire's diameter. Compared to other methods, light controlling potentially offers more freedom and flexibility, as light can be modulated not only with its intensity and direction, but also with the frequency and polarities. This nanowire motor demonstrates a step forward to harness the advantages of light, which opens up new opportunities for the realization of many novel functions such as multiple channels communication to nanorobots and controllable self-assembly.

The design and fabrication of highly functional nanomachines have been the dream and a persistent target of nanoscience for decades. Particularly, nano-/micromotors promise broad applications in biomedicine, catalysis, and environmental remediation, and have stimulated considerable research efforts over the past decades.[1–4] Artificial nano-/micromotors can be powered by varieties of energy sources such as chemical fuels,[5–8] magnetic fields,[9–11] acoustic fields,[12,13] electric fields,[14] and light.[15–23] Since light is an external power source that can be easily controlled and shaped, light powered nano-/micromotors may offer more flexibility and controllability over other energy sources.[24–26] More recently, it has been demonstrated that, by carefully designing the nanomotor, light can be utilized not

only as a power source but also as a control signal for nanomotor navigation,[27,28] which promises a new dimension for nanomotor/nanorobot design. However, most light-powered nanomotors are based on ultraviolet (UV) light-absorption materials,[29–31] which is not preferred for biological application due to the potential UV-radiation damage. To overcome this challenge, new visible/near-infrared light-driven artificial nanomotors have been developed based on thermophoresis.[19,32] However, to generate enough temperature gradient over microscopic distance for nanomotor propulsion, a high light intensity (over 10 W cm^{-2}) has to be applied, which may lead to potential heat damage to living tissues. More recently, some narrower-bandgap semiconductor nanoparticles have been utilized for visible-light-driven nanomotors, which promises potential applications in the biological field.[21,23] On the other hand, due to the perfect charge separation and strong light-trapping effect, nanowire solar cells can effectively harvest photon energy[33–35] while maintaining their miniaturized size, which makes them a perfect candidate for light-powered nanomotors. It is worth mentioning that, for nanomotors based on electrophoresis, a very low current density ($\approx$1 µA cm^{-2})[8,27] is required for the nanomotor propulsion, while a much greater photocurrent density (over 10 mA cm^{-2}) can be readily generated in a single silicon nanowire.[36] Here, we demonstrated a visible/near-infrared light-driven nanomotor based on a single silicon nanowire, which can operate under visible/near-infrared light at ultralow intensity.

Moreover, due to the strong optical resonance inside the silicon nanowire, the spectral response of the nanowire-based nanomotor can be easily modulated by controlling the nanowire's diameter.[37–39] These observations not only support our proposed propulsion mechanism but also suggest that well-established nanophotonic enhancement techniques[40,41] can be applied to the light-powered nanomotor. Compared to other controlling methods, light can be modulated not only with intensity and direction, but also with frequencies, which offers an additional dimension for nanomotor control. With the tunable spectral response of the designed nanomotor, some more advanced functions may be conceived. For example, light

J. Wang, Z. Xiong, X. Zhan, B. Dai, J. Zheng,
J. Liu, Prof. J. Tang
Department of Chemistry
The University of Hong Kong
Hong Kong 999077, China
E-mail: jinyao@hku.hk

1701451 (1 of 7)

**ADVANCED
SCIENCE NEWS**
www.advancedsciencenews.com

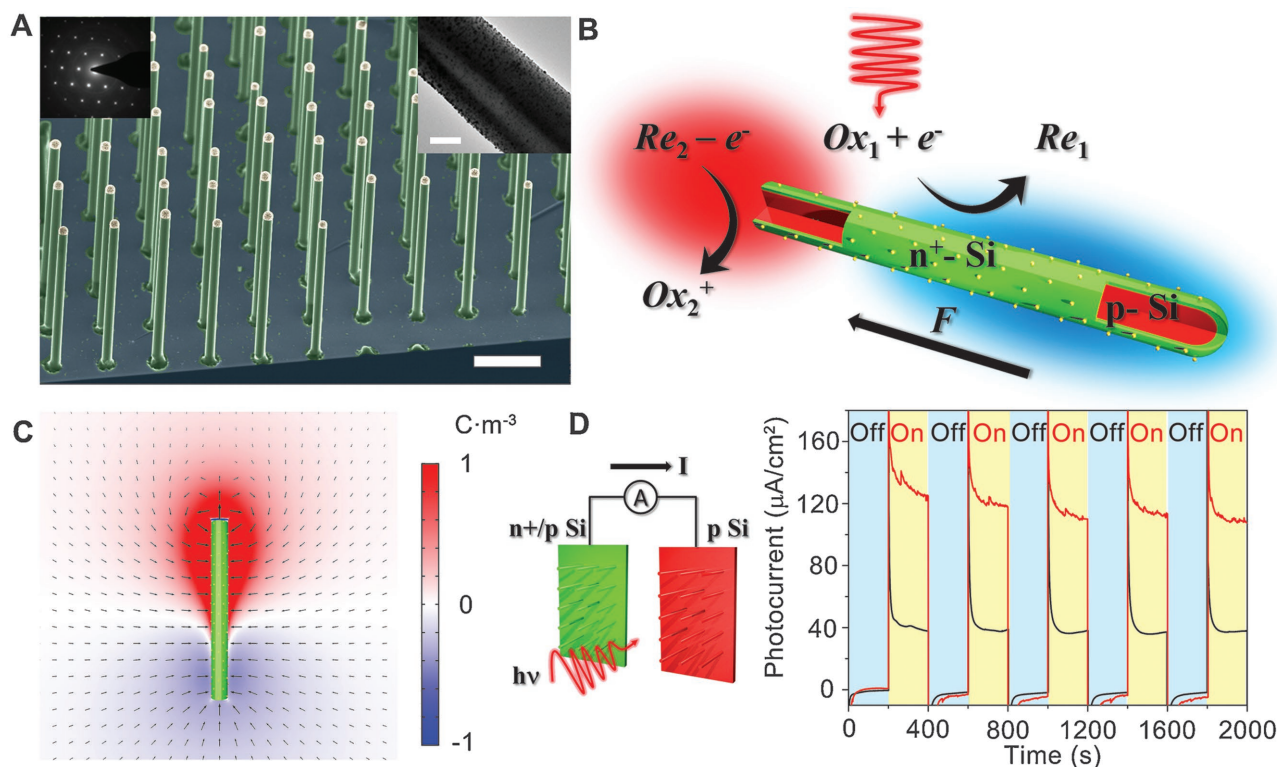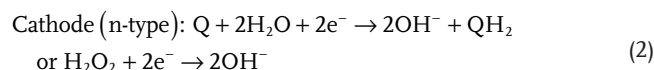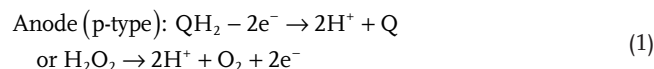**ADVANCED
MATERIALS**
www.advmat.de

Figure 1. Schematic diagram and structure characterizations of silicon nanomotor. A) False-colored scanning electron microscopy image of VLS-grown silicon wire array (scale bar: 10 μm). Inset: Transmission electron microscope image of an individual motor (upper right, scale bar: 500 nm) and selected-area electron diffraction pattern (upper left), showing the single-crystalline nature of silicon. B) Schematic diagram of the light-driven nanomotor. An n^+-Si (green) shell was formed on a p-Si core (red) by thermal diffusion doping of phosphorous. The p-Si is only exposed at one end of the nanowire, and platinum (yellow) nanoparticles were deposited on the surface as electrocatalyst. Upon illumination, redox reactions on the p- and n^+-Si surface generate H^+ and OH^- ions, respectively. The electric field generated by the unbalanced ions, in turn, propels the negatively charged silicon nanowire. C) Numerical simulation of the charge distribution (color map) and electric field (black arrows, the arrow length logarithmically represents the electric field intensity) in solution. D) Illustration of the photocurrent measurement of n^+/p-Si (phosphorus-doped over p-type silicon wire) and p-Si nanowire photoelectrodes (left image). Short-circuit current of the nanowire photoelectrodes (right image) in Q (10×10^{-3} M)/QH$_2$ (20×10^{-3} M) solution (black line) and H$_2$O$_2$ solution (0.5 wt%, red line) under chopped illumination.

with different frequencies can be projected spontaneously to multiple spectrally engineered nanomotors with corresponding wavelength response and control them independently. The spectral engineering capability demonstrated here represents a step forward to fully harness the flexibility of the light-driven nanomotor.

A large-scale silicon nanowire array was synthesized by the vapor–liquid–solid (VLS) growth method (see the Supporting Information and Figure S1, Supporting Information). **Figure 1**A shows a scanning electron microscopy (SEM) image of the as-prepared single-crystalline silicon-wire array. It has been demonstrated previously that with proper control of the growth conditions and the catalyst size, large-scale nanowires with uniform length and diameter can be obtained, which is preferred for low-cost fabrication of the nanomotors.[42] Figure 1B shows a schematic diagram of a nanomotor based on a core–shell silicon nanowire, wherein an n^+-Si shell (green) is formed on the surface of a p-type Si nanowire (red) by gas-phase diffusion doping of phosphorous, while the p-Si is only exposed at one end of the nanowire. After preparing the array of core–shell nanowires, platinum (yellow) nanoparticles were deposited as electrocatalyst on the surface of n^+-Si by sputtering

and electroless deposition (Figure 1A, inset transmission electron microscopy (TEM) image). A two-electron/hole scavenger couple, 1,4-benzoquinone/hydroquinone (Q/QH$_2$) and H$_2$O$_2$, was utilized as a redox shuttle to illustrate the self-electrophoretic propulsion mechanism of our nanomotor. Upon illumination, a photovoltage is generated across p–n junction of silicon nanowire, which drives the electrochemical redox reaction and produces positively charged proton (H^+) and negatively charged hydroxide (OH^-) on the p-type core and n-type shell, respectively, as shown in Equation (1) and (2):

$$\text{Anode (p-type): } QH_2 - 2e^- \rightarrow 2H^+ + Q$$
$$\text{or } H_2O_2 \rightarrow 2H^+ + O_2 + 2e^- \tag{1}$$

$$\text{Cathode (n-type): } Q + 2H_2O + 2e^- \rightarrow 2OH^- + QH_2$$
$$\text{or } H_2O_2 + 2e^- \rightarrow 2OH^- \tag{2}$$

The reaction generates unbalanced ion gradient and an electric-field distribution around the nanowire, as illustrated by the numerical simulation results in Figure 1C (COMSOL Multiphysics, see the Supporting Information for details). Since
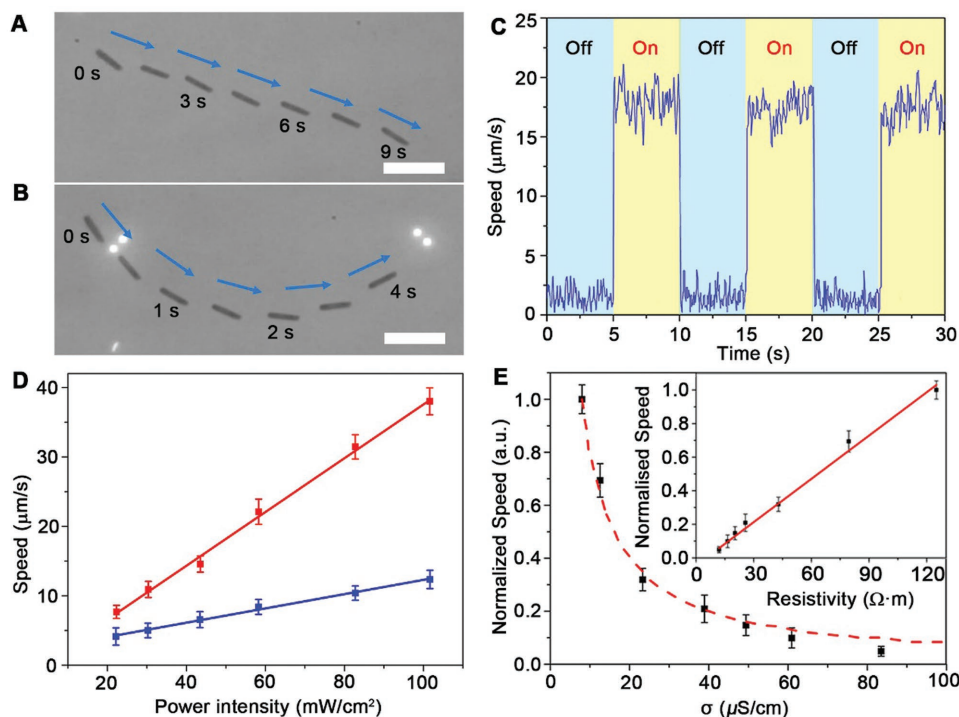
Figure 2. Individual nanowire migration under visible-light illumination. Superimposed images of sequential frames show the migration of the same nanowire in: A) Q $(10 \times 10^{-3}$ M$)$/QH$_2$ $(20 \times 10^{-3}$ M$)$ solution and in B) H$_2$O$_2$ solution (0.5 wt%) under the same illumination conditions. The scale bars are 20 μm. C) The typical nanowire migration speed under chopped light illumination. D) The nanowire migration speed scales linearly with incident illumination intensity. For the same nanowire, the migration speed is higher in H$_2$O$_2$ solution (red) than in Q/QH$_2$ solution (blue), due to fast redox kinetics. E) Normalized migration speed versus solution conductivity of the experiment data (black square points) and theoretical curve (the red dashed line is a fit curve of the form $\nu_e \propto 1/\sigma$). Inset: normalized migration speed versus solution resistivity.

the silicon nanowire surface is negatively charged (zeta potential ≈ −20 mV),[27] the electric field established by the unbalanced H$^+$ and OH$^-$ distribution propels the nanowire toward the exposed p-type silicon end. The electrical current flow inside the motor generated by the photoinduced reaction is confirmed by photocurrent measurement on separated n$^+$/p-Si photocathode and p-Si photoanode (Figure 1D).

In our experiment, a halogen lamp equipped with a 450 nm long-pass filter is utilized as the broadband visible-light illumination source. Two redox couples, Q $(10 \times 10^{-3}$ M$)$/QH$_2$ $(20 \times 10^{-3}$ M$)$ and 0.5 wt% H$_2$O$_2$ in aqueous solution, are used as the redox shuttle. **Figure 2**A,B shows the trajectory of the same nanowire in Q/QH$_2$ and H$_2$O$_2$ solution, respectively. Due to the faster reaction kinetics, the faster nanowire migration in the H$_2$O$_2$ solution is observed compared to the same nanowire migration in Q/QH$_2$ solution. In the dark or without redox shuttle, the photoelectrochemical reaction is switched "OFF" and only Brownian motion of the nanowires is observed (Movie S1, Supporting Information). Upon illumination, the photoelectrochemical reaction is switched "ON" and the nanowire begins to migrate (Figure 2C, and Movie S2, Supporting Information).

Since the core–shell silicon nanowire can effectively harvest energy from the incident photons, our silicon nanomotor can operate under an ultralow light intensity, which is highly desired for the biological application. Particularly, the nanowire migration speed can reach 9.6 μm s^{-1} at the light intensity of ≈3 mW cm^{-2} (Movie S3, Supporting Information). As shown

in Figure 2D, the migration speed of the nanowire scales linearly with the incident light intensity, which supported our light-driven electrophoresis propulsion mechanism. The intrinsic swimming mobility of the nanowire can be quantified by the light-intensity-normalized-migration velocity (LINMV), which is the slope of the absolute migration speed as a function of light intensity.[27] Due to faster electrochemical reaction kinetics in H$_2$O$_2$, as measured in photocurrent measurement (Figure 1D), the LINMV in H$_2$O$_2$ is 38.7 ± 4.3 mm^3 J^{-1} (95% confidence interval) which is higher than the LINMV in Q/QH$_2$, which is 10.27 ± 3.4 mm^3 J^{-1} (95% confidence interval). It is well known that due to the ionic screening of the induced electric field, the self-electrophoresis-based nanomotor suffers from a deteriorated propulsion speed in media with increased electrolyte concentration, such as in biological media. To further confirm the self-electrophoretic mechanism, as well as study the ionic screening effect for our nanowire, the correlation between solution conductivity and migration speed is also explored. The in situ migration speed of the same silicon nanowire was measured in solutions with different ionic strengths, using a testing stage integrated with a customized electrical-conductivity meter. Figure 2E shows the reciprocal dependence of normalized experimental nanowire migration speed to the solution conductivity, which is consistent with the theoretical prediction for electrophoresis mechanism.[43] This result also shows that further study and more advanced designs will be needed to increase the electrolyte concentration
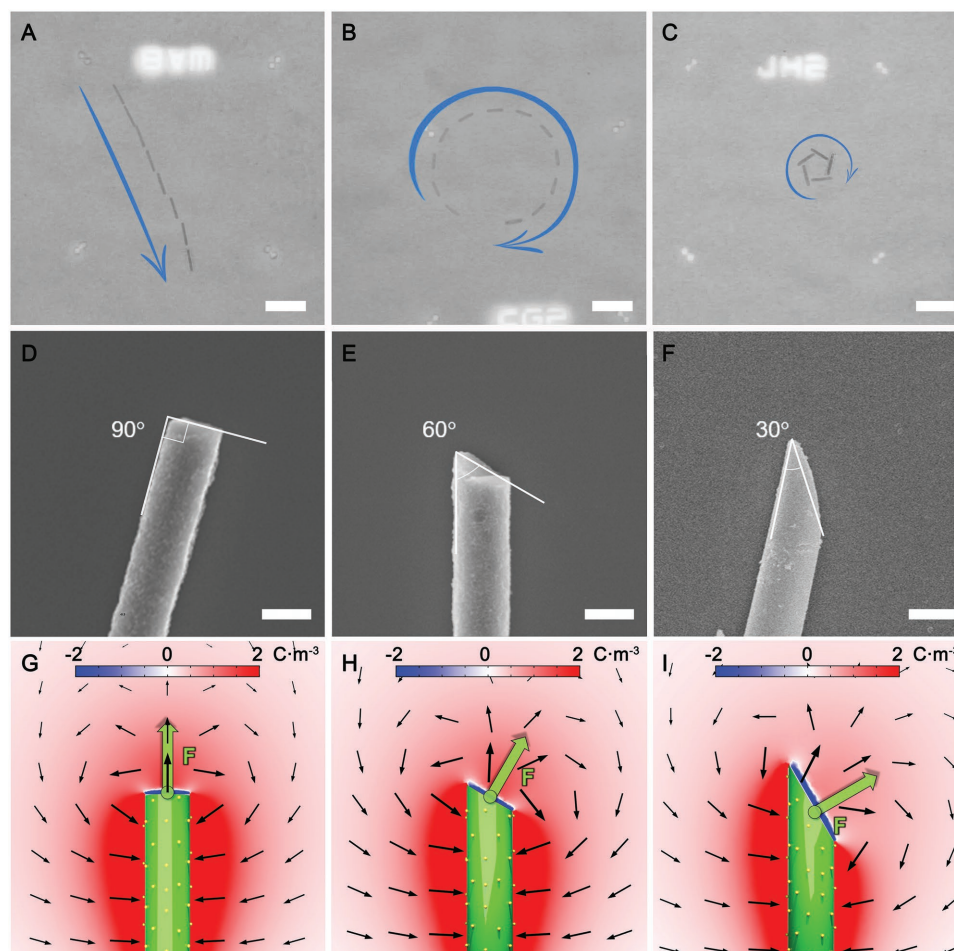
ADVANCED
SCIENCE NEWS

www.advancedsciencenews.com

ADVANCED
MATERIALS

www.advmat.de

Figure 3. Different motion trajectories induced by different nanowire end surface morphology. A–C) Superimposed images of sequential frames of nanowires with different motion trajectories: "linear," "circular," and "rotational." The scale bar is 20 µm. D–F) SEM images of different nanowire p–n junction ends correspond to three different migration trajectories. The scale bar is 500 nm. G–I) Numerical simulation of charge distribution (color map), the electric field (black arrows, the arrow length logarithmically represents the electric field intensity) of different nanowire ends. The green arrow denotes the repelling force direction exerted on end surface by surrounding solutions.

tolerance of our nanomotor before it can be applied in biological media.

We also systematically examined the structure-to-motion relationship of the nanowires and found a vital role of the detailed morphology near the exposed p–n junction to the nanomotor migration trajectory. As shown in **Figure 3**A–C, three distinct migration trajectories, namely, "linear," "circular," and "rotational," with increasing angular speed can be observed in our nanowire motor (Movie S4, Supporting Information). As described previously, the electric force applied to the whole nanowire surface propels the nanowire and is responsible for its translational migration. However, since the nanowire is simply mechanically scraped off from the VLS growth wafer by a razor blade, the fractured surface is not always normal to the nanowire growth direction. After examination of the detailed fracture surface of nanowires, it is observed that nanowires with a linear migration trajectory have the fracture surface vertical to nanowire growth direction while a more off-vertical fracture surface leads to a more rotational trajectory. As a result, we attribute the torque accountable to the angular speed of our

nanowire to the nonvertical p–n junction at the nanowire end, which leads to a highly unbalanced ion distribution around the nanowire end. As shown in Figure 3D–I, the simulated charge distribution around the exposed nanowire p–n junction, as well as the corresponding scanning electron microscopy (SEM) images, clearly demonstrated the strong electric force away from the nanowire axis. For the p-type silicon surface vertical to the axis of the nanowire (Figure 3D), the H^+ is symmetrically distributed around nanowire axis (Figure 3G), which leads to an electric force along the nanowire axis and the nanowire's linear migration. When the p-type silicon surface gradually deviates from the perpendicular position (Figure 3E,F), an asymmetric H^+ distribution around the nanowire tip is generated. The Coulombic repulsion between the localized H^+ ions and the positively charged p-type photoanode due to photovoltaic effect will apply an electric force on the p-type surface (Figure 3G–I). This force steers the nanomotor, creating a rotational torque and the circular or rotational motion accordingly.

Similar to a previously studied nanorotor,[44] the ratio (γ) between the perpendicular component of the propulsion force

(F_p) and the parallel component of the propulsion force (F_n) to the nanowire can be estimated as follows:

$$\gamma = \frac{F_p}{F_n} = \frac{a_p}{a_n} \tan\varphi \qquad (3)$$

where a_p and a_n are the shape parameters, which can be calculated modeling our nanomotor as a prolate spheroid (see the Supporting Information for details), and φ is the angle between the symmetry axis of nanowire and the translational motion direction. An analysis of the quasicircular path of "rotational" motor (Figure 3C) gives an angle of $\varphi \approx 37°$ (Figure S3, Supporting Information). Using the dimension of the nanowire (length of 10.3 µm and diameter of 800 nm) we can obtain a ratio of $\gamma \approx 1.1$. Since the F_p is largely focused on the fractured p-type silicon nanowire surface while the F_n is evenly distributed on the whole n-type silicon nanowire surface, this result indicates that, although the exposed p-type silicon area only constitutes 2–5% of the total surface area, the asymmetric electric field induced by it provides a significant perpendicular force component F_p to rotate the motor, which is comparable to the parallel force component and can account for up to ≈50% of the total force. In our core–shell nanowire, the anodic reaction is highly concentrated on the p-type silicon end, subsequently producing a large electric field and force applied to the nanowire. This result implies that the detailed structure of the nanomotor around the most concentrated reaction site plays a critical role in nanomotor migration behavior and must be carefully controlled when designing a nanomotor.

One major advantage of using light to propel/navigate nanomotor is that light with different frequencies can be supplied to the nanomotor, which offers many opportunities if nanomotors with different spectral responses can be designed. It is well known that the nanowire structure can dramatically enhance the light absorption by the light-trapping effect and can be used for high-performance solar cells.[37,45,46] Since our nanowire-based nanomotor is propelled by the photocurrent-driven electrochemical reaction, it can also be spectrally engineered by tuning the nanowire diameter. To investigate the wavelength dependence of the nanowire migration speed, we measured the migration speed of the individual nanowire under tunable wavelength illumination from 500 to 800 nm. The normalized nanowire speed is calculated after normalizing the raw migration speed by the incident photon flux at the corresponding wavelength.

In order to correlate the nanowire absorption spectra with its migration speed, the exact nanowire diameter needs to be obtained. In our synthesis process, although good uniformity of nanowire diameter can be obtained, some diameter variation is still observed (Figure S2, Supporting Information). In order to accurately measure the diameter of the tested nanowire, the nanowire after speed test is immobilized by slowly evaporating
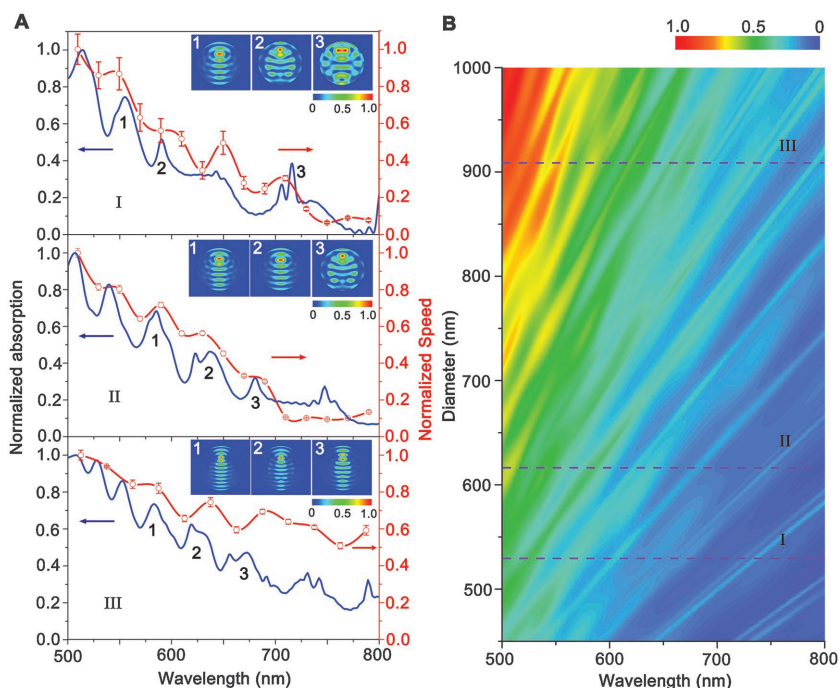

Figure 4. Wavelength-dependent motor migration speed and nanowire light absorption. A) Experimental speed normalized by photon flux at corresponding wavelength and the simulated light absorption calculated by FDTD for nanomotor with diameter of 529 nm (I), 616 nm (II), and 909 nm (III). Insets: FDTD simulations of the spatial profiles of optical absorption mode correspond to the absorption peaks denoted by numbers in the simulated absorption spectra. B) FDTD simulated absorption plot as a function of wavelength and nanomotor diameter. The dashed lines represent the calculated results shown in (A).

the solution, and the location of the tested nanomotor can be identified with the help of prepatterned markers on the testing stage. The diameter of the tested nanowire is then measured by high-resolution SEM and adopted for finite difference time domain (FDTD) simulation. It is well known that the FDTD simulation can provide accurate absorption spectra of nanowires, as demonstrated in a single-nanowire photodetector and solar-cell measurement.[37–39] As shown in **Figure 4**A, the nanowire spectral response matches very well with the simulated absorption spectra, verifying that the photocurrent and the self-electrophoresis is essential for propelling nanomotor. It is worth noting that for a large-diameter nanowire (909 nm diameter), the long-wavelength response seems to deviate from the simulated absorption. This deviation is due to the higher internal quantum efficiency for long-wavelength photons in large-diameter silicon nanowires similar to that of the bulk silicon solar cell and can be eliminated by proper surface passivation.[47] To give an overview of the spectral response of the silicon-nanowire migration, the absorption spectra were systematically explored by FDTD simulation (Figure 4B), which provides guidance for controlling the motion by engineering the diameter of the nanowire.

In summary, we have successfully demonstrated a light-powered silicon nanowire-based nanomotor that can be propelled by ultralow-intensity visible or near-infrared illumination. We find that significant propulsion force is concentrated around the exposed p–n junction area, implying the prospect of adjusting migration behavior of the nanomotor through

altering the detailed structure around the p–n junction. Finally, by utilizing the optical resonance in the nanowire, the spectral response of nanowire motor can be controlled, which offers a new protocol for nanomotor design. It can be foreseen that versatile functionality can be realized by carefully integrating the photonic structure into the optically powered nanorobot where optical input with different light frequencies can be used for complex maneuvers.

Experimental Section

Nanomotor Synthesis and Measurement: The structure of the motor is based on a core–shell p–n junction silicon nanowire with platinum catalyst on the surface. The silicon wire array was prepared by the VLS growth process with a patterned substrate. The n^+-Si shell was produced by the thermal diffusion method. Typically, a Si handle wafer with spin-coated P450 phosphorus dopant (Filmtronics, Inc.) was used as a phosphorus source. The Si-nanowire-array sample was placed directly underneath the handle wafer with 400 µm distance under rough vacuum with 55 sccm H_2/Ar gas (1:10, v/v) flow. Then the wafer temperature was quickly raised to 900 °C by pushing the wafers into preheated furnace and annealed for 3 min. After BHF treatment, 1 nm platinum nanoparticles were loaded on the surface of the silicon nanowires as catalysts by magnetron sputtering. Before the motion measurement, the catalysts needed to be activated by 0.5×10^{-3} M chloroplatinic acid (H_2PtCl_6) (Sigma–Aldrich) and 0.5 M HF solution.

The as-prepared nanowires could be scraped off from the silicon wafer and transferred into H_2O_2 or Q/QH_2 solution for measurement. The nanomotor motion was observed and recorded using an Olympus MX51 optical microscope and a Canon EOS 60D digital camera. In the spectral-response measurement, a supercontinuum laser (SC-Pro, Wuhan Yangtze Soton Laser Co., Ltd.) coupled to a variable linear filter was used as the light source for the wavelength-dependent measurements ranging from 500 to 800 nm. After measurement, the nanomotor was immobilized on the surface after slowly evaporating the solution. The detailed structure of the tested nanowire was examined by SEM to discover its correlation with the migration behavior. A microscope halogen lamp with a 450 nm long-pass filter was used as the light source for the "ON–OFF" motion, light-intensity dependence, and solution-conductivity-dependence measurements. More details for the sample preparation and measurements can be found in the Supporting Information.

Photocurrent Measurement: A two-electrode photochemical measurement setup was used to determine the photocurrent of n^+/p-Si electrodes in H_2O_2 solution and Q/QH_2 solution. A piece of doped n^+/p-Si wafer and a piece of p-Si wafer loaded with platinum nanoparticles were used as photocathode and photoanode with the exposed area ratio of 40:1 to mimic the cathode-to-anode ratio in the nanowire. The two separated electrodes were immersed in 1,4-benzoquinone (10×10^{-3} M)/hydroquinone (20×10^{-3} M) or 0.5 wt% H_2O_2 and 1 M KCl aqueous solution, and connected to a Keithley 2635B sourcemeter (Tektronix, Inc.) for short-circuit current measurement.

Numerical Simulation: The simulation was conducted using the commercial FDTD software package (Lumerical Solutions, Inc.). The diameter of the nanowire was adopted from SEM image after recording the motion behavior. The simulation space was 5 µm × 5 µm × 5 µm with perfectly matched layer boundaries along the x-, y-, and z-axes. The light source was a plane wave propagating along the minus z-direction with wavelength from 500 to 800 nm. The mesh was the nonuniform type with an accuracy of 3. The absorption spectra were calculated using a 2D cross-section monitor. COMSOL Multiphysics (version 5.2) was used to solve the H^+ and OH^- concentration, the charge distribution, and the electric field. 3D simulations were used for rod-shaped Si nanomotors. Outside Si nanomotor, a cylinder of fluid was placed (50 µm in length and 25 µm in diameter). The anode (H^+) and cathode (OH^-) fluxes on

the nanowire surface were set according to the measured photocurrent. The H^+ and OH^- flux were kept to be equal in value on both ends at all times to conserve charge neutrality. A predefined finer mesh for fluid hydrodynamics was used for the fluid domain. A fine mesh condition was chosen at the end of Si nanomotor to clarify the charge distribution. A free tetrahedral mesh was used to generate 117 431 elements. A stationary simulation was carried out to calculate the system at steady state.

Supporting Information

Supporting Information is available from the Wiley Online Library or from the author.

Conflict of Interest

The authors declare no conflict of interest.

[1] J. Wang, W. Gao, *ACS Nano* **2012**, *6*, 5745.

[2] D. Patra, S. Sengupta, W. Duan, H. Zhang, R. Pavlick, A. Sen, *Nanoscale* **2013**, *5*, 1273.

[3] J. G. S. Moo, M. Pumera, *Chem. Eur. J.* **2015**, *21*, 58.

[4] W. Wang, W. Duan, S. Ahmed, T. E. Mallouk, A. Sen, *Nano Today* **2013**, *8*, 531.

[5] S. Sengupta, K. K. Dey, H. S. Muddana, T. Tabouillot, M. E. Ibele, P. J. Butler, A. Sen, *J. Am. Chem. Soc.* **2013**, *135*, 1406.

[6] X. Ma, A. Jannasch, U.-R. Albrecht, K. Hahn, A. Miguel-López, E. Schäffer, S. Sánchez, *Nano. Lett.* **2015**, *15*, 7043.

[7] W. F. Paxton, K. C. Kistler, C. C. Olmeda, A. Sen, S. K. St. Angelo, T. E. M. Y. Cao, P. E. Lammert, V. H. Crespi, *J. Am. Chem. Soc.* **2004**, *126*, 13424.

[8] W. F. Paxton, P. T. Baker, T. R. Kline, Y. Wang, T. E. Mallouk, A. Sen, *J. Am. Chem. Soc.* **2006**, *128*, 14881.

[9] A. Ghosh, P. Fischer, *Nano Lett.* **2009**, *9*, 2243.

[10] W. Gao, X. Feng, A. Pei, C. R. Kane, R. Tam, C. Hennessy, J. Wang, *Nano Lett.* **2014**, *14*, 305.

[11] E. E. Keaveny, S. W. Walker, M. J. Shelley, *Nano Lett.* **2013**, *13*, 531.

[12] W. Wang, S. Li, L. Mair, S. Ahmed, T. J. Huang, T. E. Mallouk, *Angew. Chem.* **2014**, *126*, 3265.

[13] J. Li, T. Li, T. Xu, M. Kiristi, W. Liu, Z. Wu, J. Wang, *Nano Lett.* **2015**, *15*, 4814.

ADVANCED
SCIENCE NEWS
www.advancedsciencenews.com

ADVANCED
MATERIALS
www.advmat.de

[14] G. Loget, A. Kuhn, *Nat. Commun.* **2011**, *2*, 535.

[15] A. A. Solovev, E. J. Smith, C. C. Bof' Bufon, S. Sanchez, O. G. Schmidt, *Angew. Chem., Int. Ed.* **2011**, *50*, 10875.

[16] Y. Hong, M. Diaz, U. M. Córdova-Figueroa, A. Sen, *Adv. Funct. Mater.* **2010**, *20*, 1568.

[17] R. Dong, Q. Zhang, W. Gao, A. Pei, B. Ren, *ACS Nano* **2016**, *10*, 839.

[18] Z. Wu, X. Lin, Y. Wu, T. Si, J. Sun, Q. He, *ACS Nano* **2014**, *8*, 6097.

[19] A. P. Bregulla, H. Yang, F. Cichos, *ACS Nano* **2014**, *8*, 6542.

[20] A. A. Solovev, E. J. Smith, C. C. Bof' Bufon, S. Sanchez, O. G. Schmidt, *Angew. Chem., Int. Ed. Engl.* **2011**, *50*, 10875.

[21] D. Zhou, Y. C. Li, P. Xu, N. S. McCool, L. Li, W. Wang, T. E. Mallouk, *Nanoscale* **2017**, *9*, 75.

[22] Z. Wu, T. Si, W. Gao, X. Lin, J. Wang, Q. He, *Small* **2016**, *12*, 577.

[23] R. Dong, Y. Hu, Y. Wu, W. Gao, B. Ren, Q. Wang, Y. Cai, *J. Am. Chem. Soc.* **2017**, *139*, 1722.

[24] M. Ibele, T. E. Mallouk, A. Sen, *Angew. Chem., Int. Ed. Engl.* **2009**, *48*, 3308.

[25] W. Duan, M. Ibele, R. Liu, A. Sen, *Eur. Phys. J. E* **2012**, *35*, 77.

[26] S. Palagi, A. G. Mark, S. Y. Reigh, K. Melde, T. Qiu, H. Zeng, C. Parmeggiani, D. Martella, A. Sanchez-Castillo, N. Kapernaum, F. Giesselmann, D. S. Wiersma, E. Lauga, P. Fischer, *Nat. Mater.* **2016**, *15*, 647.

[27] B. Dai, J. Wang, Z. Xiong, X. Zhan, W. Dai, C.-C. Li, S.-P. Feng, J. Tang, *Nat. Nanotechnol.* **2016**, *11*, 1087.

[28] C. Chen, F. Mou, L. Xu, S. Wang, J. Guan, Z. Feng, Q. Wang, L. Kong, W. Li, J. Wang, Q. Zhang, *Adv. Mater.* **2017**, *29*, 1603374.

[29] F. Mou, Y. Li, C. Chen, W. Li, Y. Yin, H. Ma, J. Guan, *Small* **2015**, *11*, 2564.

[30] R. Dong, Q. Zhang, W. Gao, A. Pei, B. Ren, *ACS Nano* **2016**, *10*, 839.

[31] W. Duan, M. Ibele, R. Liu, A. Sen, *Eur. Phys. J. E* **2012**, *35*, 77.

[32] M. Xuan, Z. Wu, J. Shao, L. Dai, T. Si, Q. He, *J. Am. Chem. Soc.* **2016**, *138*, 6492.

[33] B. Tian, X. Zheng, T. J. Kempa, Y. Fang, N. Yu, G. Yu, J. Huang, C. M. Lieber, *Nature* **2007**, *449*, 885.

[34] J. Tang, Z. Huo, S. Brittman, H. Gao, P. Yang, *Nat. Nanotechnol.* **2011**, *6*, 568.

[35] S. A. Mann, S. Z. Oener, A. Cavalli, J. E. M. Haverkort, E. P. A. M. Bakkers, E. C. Garnett, *Nat. Nanotechnol.* **2016**, *11*, 1071.

[36] Y. Su, C. Liu, S. Brittman, J. Tang, A. Fu, N. Kornienko, Q. Kong, P. Yang, *Nat. Nanotechnol.* **2016**, *11*, 609.

[37] L. Cao, J. S. White, J.-S. Park, J. A. Schuller, B. M. Clemens, M. L. Brongersma, *Nat. Mater.* **2009**, *8*, 643.

[38] L. Cao, P. Fan, A. P. Vasudev, J. S. White, Z. Yu, W. Cai, J. A. Schuller, S. Fan, M. L. Brongersma, *Nano Lett.* **2010**, *10*, 439.

[39] T. J. Kempa, J. F. Cahoon, S.-K. Kim, R. W. Day, D. C. Bell, H.-G. Park, C. M. Lieber, *Proc. Natl. Acad. Sci. USA* **2012**, *109*, 1407.

[40] S. Brittman, H. Gao, E. C. Garnett, P. Yang, *Nano Lett.* **2011**, *11*, 5189.

[41] S.-K. Kim, R. W. Day, J. F. Cahoon, T. J. Kempa, K.-D. Song, H.-G. Park, C. M. Lieber, *Nano Lett.* **2012**, *12*, 4971.

[42] S. W. Boettcher, J. M. Spurgeon, M. C. Putnam, E. L. Warren, D. B. Turner-Evans, M. D. Kelzenberg, J. R. Maiolo, H. A. Atwater, N. S. Lewis, *Science* **2010**, *327*, 185.

[43] J. L. Moran, J. D. Posner, *Phys. Fluids* **2014**, *26*, 042001.

[44] A. Nourhani, Y.-M. Byun, P. E. Lammert, A. Borhan, V. H. Crespi, *Phys. Rev. E* **2013**, *88*, 062317.

[45] M. D. Kelzenberg, S. W. Boettcher, J. A. Petykiewicz, D. B. Turner-Evans, M. C. Putnam, E. L. Warren, J. M. Spurgeon, R. M. Briggs, N. S. Lewis, H. A. Atwater, *Nat. Mater.* **2010**, *9*, 239.

[46] E. S. Barnard, R. A. Pala, M. L. Brongersma, *Nat. Nanotechnol.* **2011**, *6*, 588.

[47] Y. Dan, K. Seo, K. Takei, J. H. Meza, A. Javey, K. B. Crozier, *Nano Lett.* **2011**, *11*, 2527.